Commun. Comput. Phys. Vol. **37**, No. 1, pp. 171-192
doi: 10.4208/cicp.OA-2024-0050 January 2025

Electromagnetic Gyrokinetic Simulation of Tokamak Plasma with Semi-Lagrangian Scheme

Pengfei Zhao, Xiaotao Xiao*, Qilong Ren*, Deng Zhou and Lei Ye

CAS Key Laboratory of Frontier Physics in Controlled Nuclear Fusion and Institutes of Plasma Physics, Chinese Academy of Sciences, Hefei 230031,People's Republic of China.

Received 8 March 2024; Accepted (in revised version) 8 September 2024

Abstract. The re-splitting δf method (Ye et. al CPC 2020) has been implemented into the global semi-Lagrangian gyrokinetic code NLT (Lei Ye et al. 2016, JCP) for the simulations of electromagnetic micro-turbulence in tokamak plasmas. The re-splitting method can be incorporated with the numerical Lie transform method, which is an essential numerical scheme for NLT code, to mitigate the cancellation problem appears in the gyrokinetic $p_{\|}$-formulation with gyrokinetic ions and drift-kinetic electrons. With this method, the ion temperature gradient mode (ITG), the kinetic ballooning mode (KBM) and trapped electron mode (TEM) are simulated by NLT and the results are well benchmarked with other gyrokinetic simulation codes.

AMS subject classifications: 65D05, 65Z05, 68U20, 82D10

Key words: Electromagnetic gyrokinetic, numerical Lie transform, re-splitting, semi-Lagrange.

1 Introduction

Large-scale gyrokinetic simulation has become a powerful tool to study various critical physical processes in tokamak plasmas, especially the low frequency ($\omega \ll \omega_c$) waves including but not limited to micro-turbulence and energetic particle driven modes. Here, ω and ω_c are the frequency of relevant waves and gyro-motion of particles. In gyrokinetic theory, the high-frequency gyromotion of charged particles in a magnetic field can be decoupled from the low-frequency drift motion of the gyrocenter, while essential kinetic effects are retained, like finite Larmor radius (FLR) effects and wave-particle resonance effects (through drift motion).

---

*Corresponding author. *Email addresses:* `xtxiao@ipp.ac.cn` (X. Xiao), `renql@ipp.ac.cn` (Q. Ren), `pfzhao@ipp.ac.cn` (P. Zhao), `dzzhou@ipp.ac.cn` (D. Zhou), `lye@ipp.ac.cn` (L. Ye)

It is generally accepted that the anomalous transport observed in tokamak experiments are mainly induced by the electrostatic drift-wave type turbulence, such as ion temperature gradient (ITG) mode, trapped electron mode (TEM) and electron temperature gradient (ETG) mode. Therefore, electrostatic gyrokinetic simulations can be applied to study turbulence transport, especially for low-β plasmas, where $\beta = p/(B^2/2\mu_0)$ corresponds to the ratio between plasma kinetic pressure and magnetic pressure. However, a high-β operating scenario is more appealing for economical fusion reactors because the fusion power density is roughly proportional to p^2. As the value of β increases, the magnetic component of perturbations also become increasingly important. The electromagnetic kinetic ballooning modes (KBM) or Alfv*é*nic ion temperature gradient modes (AITG) are likely to be excited due to the coupling between drift-wave and shear Alfv*é*n wave. Moreover, global shear Alfv*é*n eigenmodes, which are essentially electromagnetic waves, can also be driven unstable by the energetic particles through wave-particle resonances. Therefore, comprehensive investigations of these important physical processes call for electromagnetic gyrokinetic simulations. Consequently, development of algorithms for global gyrokinetic simulation, with fully electromagnetic and kinetic electron effects, has been an active area of research due to its significance and challenges in studying tokamak physics.

There are two major challenges confronting electromagnetic gyrokinetic simulation with (gyro/drift)kinetic electrons, which are basically originated from the huge mass ratio between ion and electron. On the one hand, the fast streaming of passing electrons along the field line can impose stringent limitation on the time step size of simulation owing to the Courant-Friedrichs-Lewy (CFL) condition. This restriction can be alleviated either by implicit electron algorithm for continuum codes [3, 10] and PIC codes [19], or by the split-weight scheme [4] or the control-variate method [14] for PIC codes. On the other hand, the well-known 'cancellation problem' [5] arises in the gyrokinetic Ampère's equation with the $p_\parallel$-formulation [13]. The adiabatic current term carried by the zeroth electron distribution function (also referred to the electron skin depth term) can induce numerical accuracy problem in many situations, such as high-β or low-n cases, and should be treated numerically with special care. Here, n is the toroidal mode number. Recently, a novel pull-back mitigation (PBM) scheme has been developed and implemented in the PIC code GYGLES, ORB5 and XGC [7, 16, 20, 23]. Additionally, a re-splitting scheme has also been proposed incorporated with the split-weight scheme and implemented in GEM code [31].

In this work, we report the recent developments for electromagnetic simulation in the semi-Lagrangian gyrokinetic code NLT [34], which is based on the numerical Lie transform method. The re-splitting scheme has been successfully implemented into the NLT code. It has been observed that this algorithm is compatible with the semi-Lagrangian scheme and effectively mitigates the cancellation problem, thereby enhancing the numerical accuracy for electromagnetic turbulence simulations.

The rest of the paper is structured as follows: in Section 2, we present the fundamental gyrokinetic equations, with special attention to the additional field equations resulting from the split-weight scheme. Section 3 describes the details of the numerical implementation. In Section 4, we conduct linear simulations of various modes, considering the effects of electromagnetic perturbation. In addition, we also provided a comparison between electromagnetic simulations and electrostatic simulations of the nonlinear evolution of ITG-dominated turbulence at low β in Section 4. Lastly, in Section 5, we summarize the main results of this work and conduct some discussions.

2 Theory model

In this section, we first present the basic gyrokinetic equations used for NLT electromagnetic simulation.

For the standard nonlinear gyrokinetic theory, the following ordering is considered

$$\frac{\omega}{\omega_{ci}} \sim \frac{\delta f}{f} \sim \frac{e\delta\phi}{T} \sim \frac{|\delta \boldsymbol{B}|}{B} \sim k_{\parallel}\rho_i \sim \varepsilon \ll 1, \quad k_{\perp}\rho_i \sim 1,$$

where ω is the characteristic fluctuation frequency. δf, $\delta\phi$ and $\delta\boldsymbol{B}$ are the fluctuation part of particle distribution function, electrostatic potential and magnetic field, respectively. ω_{ci} denotes the ion cyclotron frequency. T is the equilibrium temperature. $k_{\parallel}$ and $k_{\perp}$ are the parallel and the vertical wave vector respectively. $\rho_i = \sqrt{T_i/m_i}/\omega_{ci}$ is the ion thermal gyro-radius while ε denotes a small parameter.

Following Ref. [1] the general gyrocenter phase space Lagrangian (or the one-form) up to $\mathcal{O}(\varepsilon)$ can be written as

$$\Gamma_s = \left(e_s\boldsymbol{A} + e_s\delta\boldsymbol{A}_{gy} + m_s v_{\parallel}\boldsymbol{b}\right)\cdot d\boldsymbol{X} + \frac{\mu B}{\omega_{cs}} d\xi - H dt. \tag{2.1}$$

Here $\boldsymbol{A}$ is the equilibrium magnetic potential and the equilibrium magnetic field $\boldsymbol{B} = \nabla\times\boldsymbol{A}$. $\boldsymbol{b} = \boldsymbol{B}/B$ denotes the unit vector of magnetic field. The subscript s stands for particle species. $\boldsymbol{Z} = \left(\boldsymbol{X}, v_{\parallel}, \mu, \xi\right)$ are gyrocenter coordinates in phase space, with $\boldsymbol{X}$ the gyrocenter position, $v_{\parallel} = \boldsymbol{b}\cdot\dot{\boldsymbol{X}}$ the gyrocenter parallel velocity, $\mu = m_s v_{\perp}^2/2B$ the gyrocenter magnetic moment and ξ the gyro-angle. In this work, only shear-Alfvén perturbations, $\delta A_{\parallel}\boldsymbol{b}$ and $\delta\boldsymbol{B}_{\perp} \cong \nabla_{\perp}\delta A_{\parallel}\times\boldsymbol{b}$, are considered. Thus the symplectic-perturbation magnetic potential is

$$\delta\boldsymbol{A}_{gy} = \alpha\overline{\delta A_{\parallel}}\boldsymbol{b},$$

where $\overline{(\cdots)}$ denotes the gyro-average operator defined by

$$\overline{(\cdots)} = \frac{1}{2\pi}\oint(\cdots)\left(\boldsymbol{X} + \boldsymbol{\rho}_s(\boldsymbol{X},\mu,\xi)\right) d\xi, \tag{2.2}$$

and α is a parameter between 0 and 1. The gyrocenter Hamiltonian is composted of the zeroth order part $H_0 = \mu B + m_s v_{\parallel}^2/2$ and the perturbed part H_1, which is given by

$$H_1 = e_s\overline{\delta\phi} - e_s v_{\parallel}(1-\alpha)\overline{\delta A_{\parallel}}. \tag{2.3}$$

The gyrocenter motion equations can be obtained from the Euler-Lagrangian equation

$$\begin{aligned}\dot{\boldsymbol{X}} &= \frac{\boldsymbol{b}}{e_s B_\parallel^*}\times\left(\nabla H + e_s\frac{\partial\delta\boldsymbol{A}_{gy}}{\partial t}\right) + \frac{\boldsymbol{B}^*}{m_s B_\parallel^*}\frac{\partial H}{\partial v_\parallel} \\ &= \frac{\boldsymbol{b}}{e_s B_\parallel^*}\times\left[\mu\nabla B + \nabla\left(e_s\overline{\delta\phi} - e_s(1-\alpha)v_\parallel\overline{\delta A_\parallel}\right)\right] + \frac{\boldsymbol{B}^*}{B_\parallel^*}\left(v_\parallel - \frac{e_s}{m_s}(1-\alpha)\delta A_\parallel\right),\end{aligned} \tag{2.4}$$

$$\begin{aligned}\dot{v}_\parallel &= -\frac{\boldsymbol{B}^*}{m_s B_\parallel^*}\cdot\left(\nabla H + e_s\frac{\partial\delta\boldsymbol{A}_{gy}}{\partial t}\right) \\ &= -\frac{\boldsymbol{B}^*}{m_s B_\parallel^*}\cdot\left[\mu\nabla B + \nabla\left(e_s\overline{\delta\phi} - e_s(1-\alpha)v_\parallel\overline{\delta A_\parallel}\right) + e_s\frac{\partial\alpha\overline{\delta A_\parallel}}{\partial t}\boldsymbol{b}\right].\end{aligned} \tag{2.5}$$

Here, the effective potential and effective magnetic field is defined by $\boldsymbol{A^*} = \boldsymbol{A} + \delta\boldsymbol{A}_{gy} + \frac{m_s}{e_s}v_\parallel\boldsymbol{b}$ and $\boldsymbol{B}^* = \nabla\times\boldsymbol{A}^*$, respectively. $B_\parallel^* = \boldsymbol{B}^*\cdot\boldsymbol{b}$ is related to the phase space Jacobian of the gyrocenter transformation as $\mathcal{J} = B_\parallel^*/m_s$. The gyrocenter motion equations can also be put with the Poisson bracket as

$$\dot{Z}^i = \{Z^i, H\} + \{Z^i, Z^j\}\frac{\partial\Gamma_j}{\partial t}, \tag{2.6}$$

with the gyrocenter Poisson bracket defined by

$$\{F,G\} = \frac{e_s}{m_s}\left(\frac{\partial F}{\partial\xi}\frac{\partial G}{\partial\mu} - \frac{\partial G}{\partial\xi}\frac{\partial F}{\partial\mu}\right) + \frac{\boldsymbol{B}^*}{m_s B_\parallel^*}\cdot\left(\nabla F\frac{\partial G}{\partial v_\parallel} - \nabla G\frac{\partial F}{\partial v_\parallel}\right) - \frac{b}{e_s B_\parallel^*}\cdot\nabla F\times\nabla G. \tag{2.7}$$

Here, F and G represent two arbitrary scalars in the gyro-center coordinates.

The gyrokinetic Vlasov equation, which describes the evolution of particle distribution function in gyrocenter coordinates $F\left(\boldsymbol{X}, v_\parallel, \mu\right)$ is given by

$$\frac{\partial F}{\partial t} + \{F, H\} = 0, \tag{2.8}$$

or

$$\frac{d}{dt}F = \frac{\partial F}{\partial t} + \dot{\boldsymbol{X}}\cdot\nabla F + \dot{v}_\parallel\partial_\parallel F = 0, \tag{2.9}$$

equivalently. In δf simulations, the distribution function is decomposed into a perturbed part and a zeroth order part as

$$F\left(\boldsymbol{X}, v_\parallel, \mu, \xi, t\right) = \delta f\left(\boldsymbol{X}, v_\parallel, \mu, \xi, t\right) + F_M\left(\boldsymbol{X}, v_\parallel, \mu, \xi\right). \tag{2.10}$$

Here F_M usually takes a local Maxwellian form

$$F_M = \left(\frac{m}{2\pi T}\right)^{\frac{3}{2}} N\exp\left(-\frac{m v_\parallel^2/2 + \mu B}{T}\right) \tag{2.11}$$

with N the equilibrium density of particle. And the evolution equation for δf is given by

$$\frac{d}{dt}\delta f = -\frac{d}{dt_1}F, \tag{2.12}$$

with

$$\frac{d}{dt_1} = \dot{\boldsymbol{X}}_1 \cdot \nabla + \dot{v}_{\|1}\partial_{\|} \tag{2.13}$$

indicates the derivative along the perturbed part of the orbit induced by the turbulence field.

The perturbed electromagnetic fields are governed self-consistently by the gyrokinetic Maxwell's equations, including the quasi-neutrality equation

$$\sum_s e_s\left(\delta n_s^g + \delta n_s^p\right) = 0, \tag{2.14}$$

and the parallel Ampère's law

$$-\nabla_\perp^2 \delta A_\| + \sum_s (1-\alpha)\frac{\omega_{ps}^2}{c^2}\left\langle \overline{\delta A_\|}\right\rangle_\xi = \mu_0 \sum_s \delta j_{\|s}. \tag{2.15}$$

Here, $\delta n_s^g = \int d^6 Z \delta(\boldsymbol{X}+\boldsymbol{\rho}_s - \boldsymbol{x})\delta f_s$ denotes the perturbed gyrocenter density and δn_s^p is the well-known polarization density [18], which is written as

$$\delta n_s^p = \int d^6 Z \delta(\boldsymbol{X}+\boldsymbol{\rho}_s-\boldsymbol{x})\frac{e_s}{B}\frac{\partial F_{Ms}}{\partial \mu}\left[\delta\phi(\boldsymbol{X}+\boldsymbol{\rho}_s) - \overline{\delta\phi}(\boldsymbol{X},\mu)\right], \tag{2.16}$$

where $d^6 Z = \mathcal{J} d\boldsymbol{X} dv_\| d\mu\xi$ with $\mathcal{J}$ is the Jacobian of gyrocenter phase space and $\boldsymbol{x}$ is the particle position. $\delta j_{\|s} = \int d^6 Z \mathcal{J}_s v_\| \delta f_s \delta(\boldsymbol{X}+\boldsymbol{\rho}-\boldsymbol{x})$ denotes the perturbed gyrocenter parallel current density. The second term in Eq. (2.15), $\sum_s \frac{\omega_{ps}^2}{c^2}(1-\alpha)\left\langle\overline{\delta A_\|}\right\rangle_\xi$, is the adiabatic current (or skin depth) [11] term, where $\omega_{ps} = \sqrt{e_s^2 n_s/(m_s \varepsilon_0)}$ is the plasma oscillation frequency and

$$\begin{aligned}\left\langle\overline{\delta A_\|}\right\rangle_\xi &= -\frac{1}{n_s}\int d^6 Z \delta(\boldsymbol{X}+\boldsymbol{\rho}_s-\boldsymbol{x})\frac{v_\|^2}{B}\frac{\partial F_{Ms}}{\partial \mu}\overline{\delta A\|}(\boldsymbol{X},\mu)\\ &= \frac{1}{n_s}\int d^6 Z \delta(\boldsymbol{X}+\boldsymbol{\rho}_s-\boldsymbol{x})\overline{\delta A_\|}F_{MS}.\end{aligned} \tag{2.17}$$

There are generally two kinds of formulation of gyrocenter variables depending on the choice of parameter α, namely the $v_\|$-formulation (or symplectic-formulation) corresponding to $\alpha = 1$ and the $p_\|$-formulation (or Hamiltonian-formulation) corresponding to $\alpha = 0$, respectively. Here $p_\| = mv_\| + e_s\overline{\delta A_\|}$ is a canonical momentum for gyrocenter model with $\alpha=0$ [2]. These two coordinate systems satisfy the following transformation relationship,

$$\boldsymbol{X}\big|_{\alpha=0}=\boldsymbol{X}\big|_{\alpha=1}, \tag{2.18a}$$

$$v_{\|}\big|_{\alpha=0}=v_{\|}\big|_{\alpha=1}+\frac{e_s}{m_s}\overline{\delta A_{\|}}. \tag{2.18b}$$

Although these two sets of coordinates are equivalent theoretically, the numerical properties for numerical practice can be much different. The main difficulty faced by the $v_{\|}$-formulation is the appearance of the inductive component of the parallel electric field, $\partial A_{\|}/\partial t$, which can induce numerical instabilities with an explicit time integration scheme [8]. On the other hand, the $p_{\|}$-formulation dose not suffer form the numerical problem of the inductive parallel electric field thus has been employed by many gyrokinetic codes, including both PIC code and Eulerian code [11, 13]. However, the adiabatic current, the second term on the left-hand-side of Eq. (2.15), is introduced through the transform from the $p_{\|}$-gyrocenter coordinates back to the particle coordinates. Unfortunately, this term can cause another numerical accuracy problem, named the cancellation problem, which will be discussed in Section 3.1. In addition, the Poisson bracket with $p_{\|}$-formulation is time-independent and is consistent with that of the unperturbed guiding-center coordinates.

NLT [34] (Numerical Lie Transform) is a semi-Lagrangian δf gyrokinetic code based on the I-transform method. The electrostatic versions of NLT have been developed for adiabatic [34] and kinetic [35] electrons, respectively. Here, a brief review of the electromagnetic gyrokinetic equations with I-transform will be given. For more detailed information about I-transform, one can refer to Refs. [25–27] and Ref. [29]. It should be noted that for the electromagnetic I-transform proposed in Ref. [29], the δA transform is performed at first so that all the perturbed quantities ($\delta\phi$ and δA) in the gyrocenter one-form are moved into the Hamiltonian part. Hence the starting point for the electromagnetic I-transform is the $p_{\|}$-formulation. The basic idea of I-transform perturbation method is to transform the gyrocenter coordinate variables $\boldsymbol{Z}$ to a set of new variables $\boldsymbol{Z}_I$, so that the perturbed particle motion can be decoupled from the unperturbed part. That is to say, the one-form of gyrocenter Lagrangian and the gyrocenter motion equations will be formally identical to the unperturbed ones

$$\Gamma_{Is}=\left(e_s\boldsymbol{A}+m_s v_{\|}\boldsymbol{b}\right)\cdot d\boldsymbol{X}+\frac{\mu B}{\omega_{cs}}d\xi-H_0dt \tag{2.19}$$

and

$$\dot{Z}_I^i=\left\{Z_I^i,H_0\right\}_0, \tag{2.20}$$

where

$$\{K,G\}_0=\frac{e_s}{m_s}\left(\frac{\partial K}{\partial\xi}\frac{\partial G}{\partial\mu}-\frac{\partial G}{\partial\xi}\frac{\partial K}{\partial\mu}\right)+\frac{\boldsymbol{B}_0^*}{m_sB_{\|0}^*}\cdot\left(\nabla K\frac{G}{v_{\|}}-\nabla G\frac{K}{v_{\|}}\right)-\frac{\boldsymbol{b}}{e_sB_{\|0}^*}\nabla K\times\nabla G$$

denotes the unperturbed Poisson bracket with $\boldsymbol{B}_0^*=\boldsymbol{B}+\frac{m_s v_\parallel}{e_s}\nabla\times\boldsymbol{b}$. In comparison, Eq. (2.7) represents a more generalized guiding center Poisson bracket. When $\alpha\neq 0$, as both $\boldsymbol{B}^*$ and $B_\parallel^*$ include perturbations, the corresponding guiding center Poisson bracket, i.e., Eq. (2.7), also includes perturbations. Therefore the gyrokinetic equation can be expressed in the new coordinates as

$$\frac{d_0}{dt}\delta f_I(Z_I)\triangleq\left(\frac{\partial}{\partial t}+\dot{\boldsymbol{Z}}_{I0}\cdot\frac{\partial}{\partial \boldsymbol{Z}_I}\right)\delta f_I=0. \tag{2.21}$$

Here, $\frac{d_0}{dt}$ denotes the time derivatives along the unperturbed guiding center orbit and $\dot{\boldsymbol{Z}}_{I0}$ is the unperturbed guiding center velocity in phase space.

The contributions of the perturbed motion (field) to the gyrocenter distribution function can be recovered through the pull-back I-transform as

$$\delta f^{p_\parallel}(Z,t)=\delta f_I(Z_I,t)+G_1^i\partial_i(\delta f_I+F_M)+\frac{1}{2}G_1^j\partial_j\left(G_1^i\partial_i\right)(\delta f_I+F_M). \tag{2.22}$$

Here, the superscript $p_\parallel$ and $v_\parallel$ denotes the $p_\parallel$-formation and $v_\parallel$-formation gyrokinetic, respectively.

$$G_1^j=\{Z_I,S_1\}_0, \tag{2.23}$$

are the 1st-order generating vector fields and S_1 is the gauge function of I-transform, which is governed by the time evolution equation

$$\frac{\partial S}{\partial t}+\{S,H_0\}=H_1, \tag{2.24}$$

with $H_1=e_s\left(\overline{\delta\phi}-v_\parallel\overline{\delta A_\parallel}\right)$ the perturbed Hamiltonian of I-transform. Finally, the time evolution of the particle-field system in I-transform can be obtained by solving the self-consistent Eq. (2.14), Eq. (2.15) and Eqs. (2.20)-(2.24), with $\alpha=1$.

3 Numerical scheme

The numerical scheme for the time dependent electromagnetic gyrokinetic Vlasov equations, Eqs. (2.21) and (2.24), are generally the same with that used in the electrostatic version, which are described in Ref. [34]. The semi-Lagrangian method is applied with a four dimensional (or three dimension for gauge function) tensor-product B-spline interpolation scheme [28]. Due to the application of the I-transform, the characteristics now become the unperturbed gyrocenter orbit instead of the perturbed orbits. This property can be exploited to significantly improve the computational efficiency of the Vlasov solver, which is usually the most computational consuming ingredient in a semi-Lagrangian gyrokinetic code. On the one hand, an unperturbed orbit is determinate for given mesh grid point in phase space and time interval, so that it can be computed once in advance and saved as numerical table in the initialization stage. Thus all the computational overhead in particle pushing can be saved for the real time computations. On the other hand, a fixed-point interpolation algorithm has also been devised and implemented in NLT to greatly accelerate the high-dimensional interpolation with tensor-product B-splines [28]. In this section, the focus should be put on the numerical schemes related to the electromagnetic simulation, i.e., the re-splitting scheme and the algorithm of parallel Ampere's solver. For the details of other algorithms employed in NLT, one can refer to Refs. [32,34,35].

3.1 The re-splitting method in NLT

The parallel Ampere's equation (2.15) in $p_\parallel$-formulation mentioned in Section 2 can be simplified in the drift-kinetic electrons limit as

$$-\nabla_\perp^2\delta A_\parallel+\frac{\beta_e}{\rho_e^2}\delta A_\parallel=\mu_0\sum_s\delta j_{\parallel s}^{p_\parallel}. \tag{3.1}$$

Here

$$\delta j_{\parallel s}^{p_\parallel}=\int \mathcal{J} v_{\parallel s}\delta f^{p_\parallel}\delta(\boldsymbol{X}+\boldsymbol{\rho}_s-\boldsymbol{x})d^6Z \tag{3.2}$$

is the perturbed parallel current in $p_\parallel$-formulation and $\beta_e=\mu_0 n_e T_e/B^2$. The adiabatic current of ions, $\frac{\beta_i}{\rho_i^2}\delta A_\parallel$ (with $\beta_i=\mu_0 n_i T_i/B^2$), has been dropped due to $m_i \gg m_e$. The ratio between the physical current and the adiabatic current, $-\nabla_\perp^2\delta A_\parallel$, can be evaluated as

$$\frac{\nabla_\perp^2\delta A_\parallel}{\frac{\beta_e}{\rho_e^2}\delta A_\parallel}=\frac{(k_\perp\rho_i)^2}{\beta_e}\frac{m_e}{m_i}, \tag{3.3}$$

by assuming $T_i=T_e$. It can be seen that for low-n (toroidal mode number) perturbations with small value of $k_\perp$ or high-β plasma, e. g. $k_\perp\rho_e=0.1$ and $\beta_e=0.01$, the electron adiabatic current is much larger than the physical current due to the small electron-ion mass ratio.

Basically, the adiabatic current is originated from the choice of the equilibrium distribution function in $p_\parallel$-formulation,

$$F_M^{p_\parallel}=\left(\frac{m}{2\pi T}\right)^{\frac{3}{2}}N_e^{-\frac{\frac{1}{2m}{p_\parallel}^2+\mu B}{T}}. \tag{3.4}$$

The total distribution can be split with two equivalent approach as

$$\begin{aligned} f &= F_M^{v_\parallel}+\delta f^{v_\parallel} \\ &= F_M^{p_\parallel}+\delta f^{p_\parallel}. \end{aligned} \tag{3.5}$$

In the $v_{\|}$-formulation is, the physical current is carried exclusively by $\delta f^{v_{\|}}$ due to the velocity symmetry of $F_M^{v_{\|}}$. However, in the $p_{\|}$-formulation $F_M^{p_{\|}}$ does carry a parallel current dependent on $\delta A_{\|}$

$$\begin{aligned} J_{ad}^{p_{\|}} &= q\int \mathcal{J} v_{\|} F_M^{p_{\|}} d\xi d\mu dp_{\|} \\ &= -q\int \frac{\delta A_{\|} v_{\|}}{T} F_M^{v_{\|}} d\xi d\mu dp_{\|} \\ &= -\frac{q^2}{m} N\delta A_{\|}. \end{aligned} \tag{3.6}$$

Therefore, the perturbed distribution function $\delta f^{p_{\|}}$ must provide an opposite term to compensate the non-physical adiabatic current. Thus the real physical current carried by the charged particles can be expressed explicitly by

$$\delta j^{v_{\|}} = \delta j^{p_{\|}} - \delta j_{ad}^{p_{\|}}, \tag{3.7}$$

with $\delta j_{ad}^{p_{\|}} = J_{ad}^{p_{\|}}$ exactly. However, the adiabatic current can not be known before the parallel Ampere's equation is solved to give $\delta A_{\|}$. So $\delta j_{ad}^{p_{\|}}$ has to be contained implicitly in $\delta j_{\|}^{p_{\|}}$, which is calculated out by numerical integration of distribution function or particle deposition in continuum or PIC code, respectively. If $J_{ad}^{p_{\|}}$ on the L.H.S of Ampere's law. Eq. (3.1) is taken the analytical form, the discretization errors of two adiabatic current, $\delta j_{ad}^{err} = J_{ad}^{p_{\|}} - \delta j_{ad}^{p_{\|}}$, will be introduced due to the inexact cancellation of the numerical term and the analytical one. In the case of low-n or high-β simulations, δj_{ad}^{err} can be even greater than the physical current $\delta j_{\|}^{p_{\|}}$ and cause the numerical accuracy problem, which is usually named the 'cancellation problem'. For Eulerian gyrokinetic code with fixed phase space grid, the most immediate solution is to replace the analytical form of $J_{ad}^{p_{\|}}$ with its numerical form Eq. (3.6) and apply the same numerical quadrature scheme of $\delta j_{ad}^{p_{\|}}$ in Eq. (3.2). For the PIC code, however, the particle deposition position changes with the motion of markers so that an iterative Ampere's solver has been proposed to address the cancellation problem therein. Another remedy is the 're-splitting' scheme [31], which has been implemented in the gyrokinetic PIC code GEM with the local flux-tube model and successfully benchmarked against the split-weight scheme and pull-back mitigation (PBM) scheme [17, 20, 22, 23]. Here we apply this scheme in the semi-Lagrangian code NLT for the global electromagnetic gyrokinetic simulation. The basic idea of the re-splitting method is to find an reasonable prediction for $\delta A_{\|}$, named δA_D, at first and then take coordinate transform to make the adiabatic current as small as possible. $\delta A_{\|}$ can be split into two parts

$$\delta A_{\|} = \delta A_{\|}^{D} + \delta A_{\|}^{R}. \tag{3.8}$$

Hence the distribution function can be transformed accordingly to the p_R-formulation as

$$\delta f^{p_R} = \delta f^{p_{\|}} - \frac{q\delta A_{\|}^{D} v_{\|}}{T} F_M^{v_{\|}}. \tag{3.9}$$

With this transform, the parallel Ampere's equation can be cast into

$$-\nabla_\perp^2 \delta A_\| + \frac{\beta_e}{\rho_e^2}\delta A_R = \mu_0 \sum_s \delta j_{\|s}^{p_R}. \tag{3.10}$$

Here,

$$\delta j_\|^{p_R} = \int \mathcal{J} p_R \delta f^{p_R} \delta(\boldsymbol{X}+\boldsymbol{\rho}-\boldsymbol{x}) d^6 Z. \tag{3.11}$$

It can be seen that as long as $\delta A_\|^D$ is close enough to $\delta A_\|$ so that $\delta A_\|^R \ll \delta A_\|$, the adiabatic current can be greatly reduced and the cancellation problem can be mitigated consequently. Specifically, if the prediction $A_{\|D}$ happens to be $A_\|$, the Ampere's equation in $v_\|$-formulation is recovered and there is no cancellation errors anymore. An advisable choice for numerical practice in each time interval $t\in[t^n, t^{n+1}]$ can be the known perturbed magnetic vector in the last time step,

$$\delta A_\|^D = \delta A_\|(t^n). \tag{3.12}$$

It can be evaluated that the typical time step in electromagnetic gyrokinetic simulation, $\Delta t \sim 1/\omega_{ci}$, is much smaller than the time scale of perturbations. Therefore,

$$\left| \frac{\delta A_\|(t^{n+1}) - \delta A_\|^D}{\delta A_\|(t^{n+1})} \right| \sim \frac{\omega}{\omega_{ci}} \ll 1 \tag{3.13}$$

is satisfied with ω the frequency of perturbations.

3.2 The discretization of the parallel Ampere's equation

NLT employs the field-aligned coordinates for the simulation of tokamak plasma to minimize the number of grid points. The field-aligned coordinates are defined by

$$x = r, \tag{3.14}$$

$$y = q\theta - \zeta, \tag{3.15}$$

$$z = \theta. \tag{3.16}$$

Here, r is the minor radius. θ and ζ are poloidal and toroidal angle. $q(r)$ is the safety factor. The parallel gradient operator can be expressed as

$$\boldsymbol{b}\cdot\nabla = \nabla_\| = \frac{1}{JB}\frac{\partial}{\partial z}, \tag{3.17}$$

with $J = |\nabla x \times \nabla y \cdot \nabla z|^{-1}$ the Jacobian of the coordinates. The perpendicular Laplacian operator can be simplified in the field-aligned coordinates as

$$\nabla\cdot\nabla_\perp = c_1 \frac{\partial^2}{\partial x} + c_2 \frac{\partial^2}{\partial y} + c_3 \frac{\partial^2}{\partial x \partial y} + c_4 \frac{\partial}{\partial x} + c_5 \frac{\partial}{\partial y}, \tag{3.18}$$

with

$$c_1 = g^{xx}, \tag{3.19}$$

$$c_2 = g^{yy}, \tag{3.20}$$

$$c_3 = 2g^{xy}, \tag{3.21}$$

$$c_4 = \frac{1}{J}\left[\partial_x(Jg^{xx}) + \partial_z(Jg^{zx})\right], \tag{3.22}$$

$$c_5 = \frac{1}{J}\left[\partial_x(Jg^{xy}) + \partial_z(Jg^{zy})\right]. \tag{3.23}$$

Here, $g^{\alpha\beta}(x,z) = \nabla\alpha \cdot \nabla\beta$ are the metric coefficients. Note that all the partial derivatives, $\partial_z \delta A_{\|}$, has been dropped with the high-n approximation and $k_{\|} \ll k_{\perp}$. In tokamak configurations, The Fourier transform can be applied for any perturbation quantity owing to the toroidal symmetry of the equilibrium magnetic field,

$$Q(x,y,z) = \sum_n \hat{Q}_n(x,z) e^{iny}. \tag{3.24}$$

Therefore, for given toroidal mode n and z-grid z_i, the parallel Ampere's equation can be transformed into a set of complex ODEs as

$$c_1 \frac{\partial^2}{\partial x} + (inc_3 + c_4)\frac{\partial^2}{\partial x} - n^2 c_2 + inc_5. \tag{3.25}$$

4 Simulation results

In this section, we conduct a series of both linear and nonlinear simulations to validate the code implementation. The linear simulations encompass ion temperature gradient (ITG), trapped electron mode (TEM), and kinetic ballooning mode (KBM), while the nonlinear simulations focus on electromagnetic ITG turbulence under low β condition. To enable meaningful comparisons, we utilize the well-established Cyclone Base Case parameters outlined in Ref. 12. Our study centers on a concentric circular tokamak configuration characterized by a major radius of $R_0 = 1.67$m, a minor radius of $a = 0.60$m, and an inverse aspect ratio of $\epsilon = 0.36$. The equilibrium magnetic field on the magnetic axis is $B_0 = 2.0$T, and the safety factor profile is analytically expressed as

$$q = 2.52(r/a)^2 - 0.16(r/a) + 0.86, \tag{4.1}$$

where r represents the small radius. Additionally, the radial profiles of plasma are defined by

$$\frac{A(r)}{A(r_0)} = \exp\left[-\kappa_A \frac{a}{R_0} \Delta A \tanh\left(\frac{(r-r_0)/a}{\Delta A}\right)\right], \tag{4.2}$$

where A denotes the plasma temperature T or the density N. The specific values for $T_{i,e}(r_0)$ and $N_{i,e}(r_0)$ are 2.14keV and $4.66 \times 10^{19}/m^3$, respectively, with $r_0 = 0.5a$. We set the characteristic width $\Delta A = 0.3$ and choose $\kappa_T = 6.96$ and $\kappa_N = 2.23$. Consequently, we obtain peaked gradient profiles of A centered at r_0.

4.1 Linear simulation

In order to maintain consistency with the work by Ref. 12, all simulations in this subsection employ a proton-electron mass ratio of $m_p/m_e=918$. The simulation box size is defined as $l_z\times l_{v_\parallel}\times l_\mu=2\pi\times 4v_t\times 16T/B_0$, with grid resolutions set to $n_z\times n_{v_\parallel}\times n_\mu=32\times 64\times 16$. The radial size of the box and the corresponding resolution are adjusted for different toroidal mode numbers n to accurately handle the kinetic effects of passing electrons around the rational surface. For simplicity, we vary l_x vary from $80\rho_i$ to $20\rho_i$ with $n_x=512$ as the toroidal mode number n varies from 5 to 65. The simulation time step for linear simulations is set to $\Delta t=2/\omega_{ci}$.

Fig. 1 illustrates the β scanning of the mode with a fixed toroidal mode number of $n=19$. The NLT results exhibit good agreement with those obtained from GENE [12], in terms of growth rate, frequency, and the ITG-KBM transition threshold. It is widely recognized that finite β has a stabilizing influence on the ITG mode and a destabilizing effect on the KBM mode. As shown in Fig. 1(a), with an increase in normalized plasma pressure β, the most unstable ion mode undergoes a transition from ITG to KBM. The fact that the frequency of KBM is much larger than that of ITG is a distinguishing feature, as presented in Fig. 1(b).

Following this, we perform a set of $k_y\rho_i$ scans with fixed β=1%, where $k_y=nq/r$. Fig. 2 shows the frequency and linear growth rate versus $k_y\rho_i$. The results of NLT and GENE are in good agreement, indicating a transition from ITG to TEM as $k_y\rho_i$ increases. Figs. 3(a) and 3(b) show the two-dimensional mode structures of the electrostatic potential and parallel vector potential of the ITG mode for $n=25$. While Figs. 4(a) and 4(b), as well as

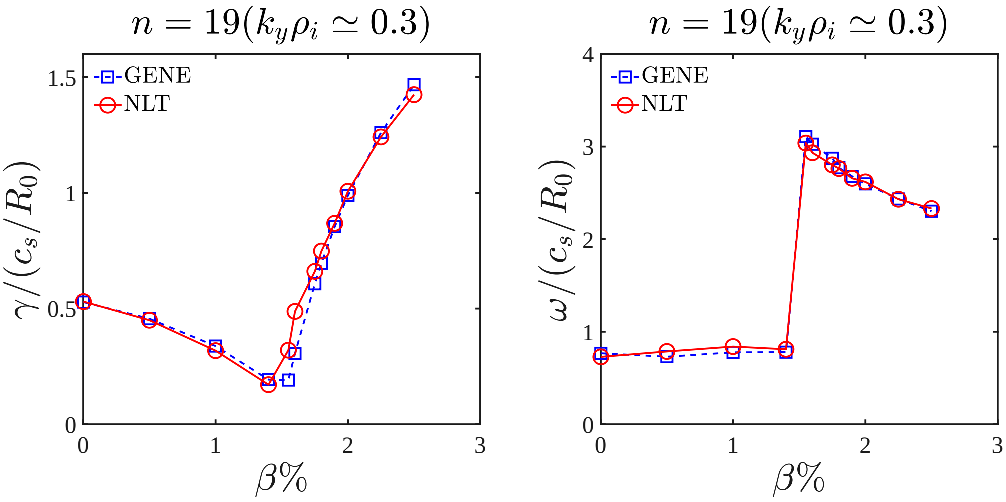

(a) (b)

Figure 1: Linear ITG-KBM simulation results from NLT and GENE for (a) growth rate and (b) real frequency with fixed toroidal mode number $n=19$. The simulation data of GENE code are taken from Ref. [12].

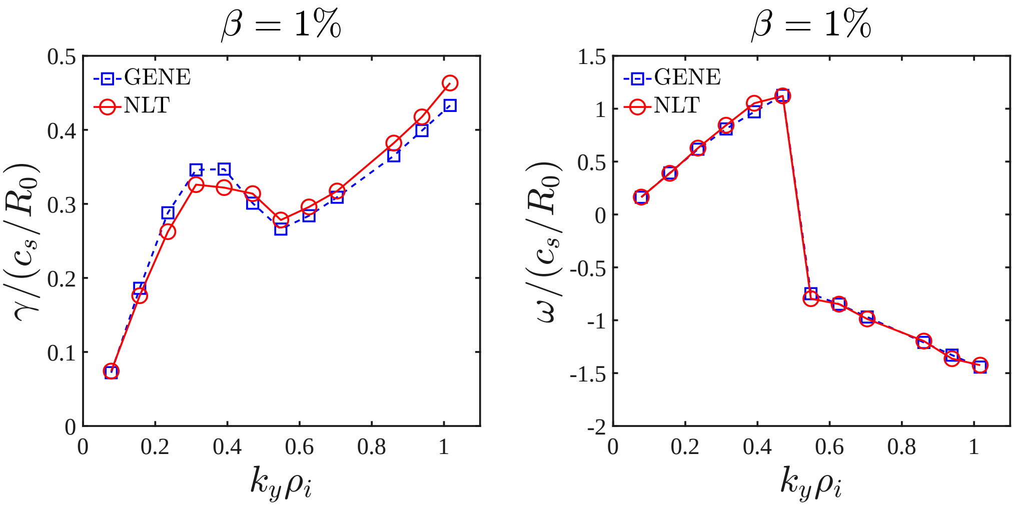

(a) (b)

Figure 2: Linear ITG-TEM simulation results from NLT and GENE for (a) growth rate and (b) real frequency for the $\beta = 1\%$ case. GENE's data are from Ref. [12].

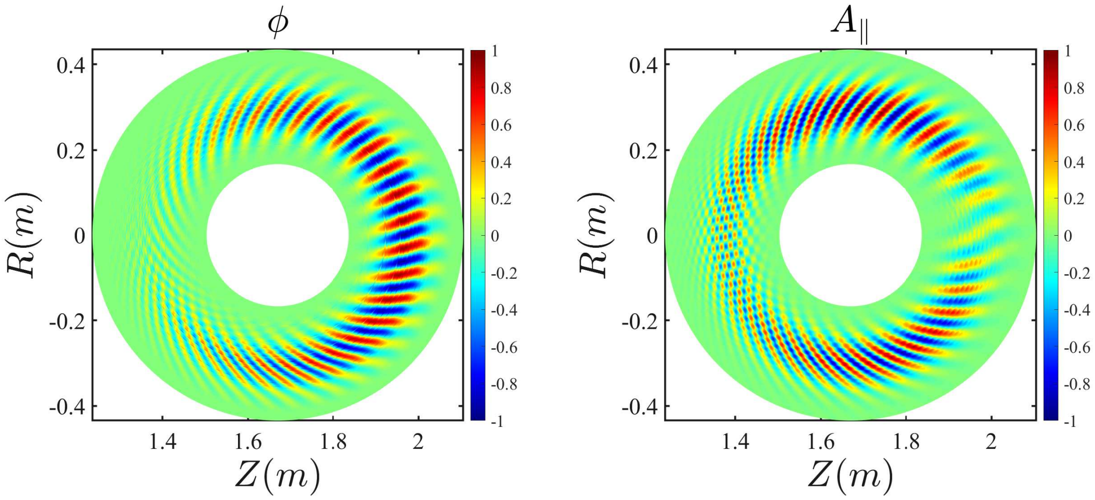

(a) (b)

Figure 3: 2D mode structure of the electrostatic potential (a) and parallel vector potential (b) in the (R,Z) plane for the case of $n = 25$ with $\beta = 1\%$.

Figs. 4(c) and 4(d), respectively, demonstrate the corresponding one-dimensional radial and polar mode structures. The mode structures given by NLT and GENE are in well agreement by comparing the above 1d and 2d mode structures with Figures 11 and 12 in Ref. [12]. Moreover, the fine structures formed by the non-adiabatic response of electrons

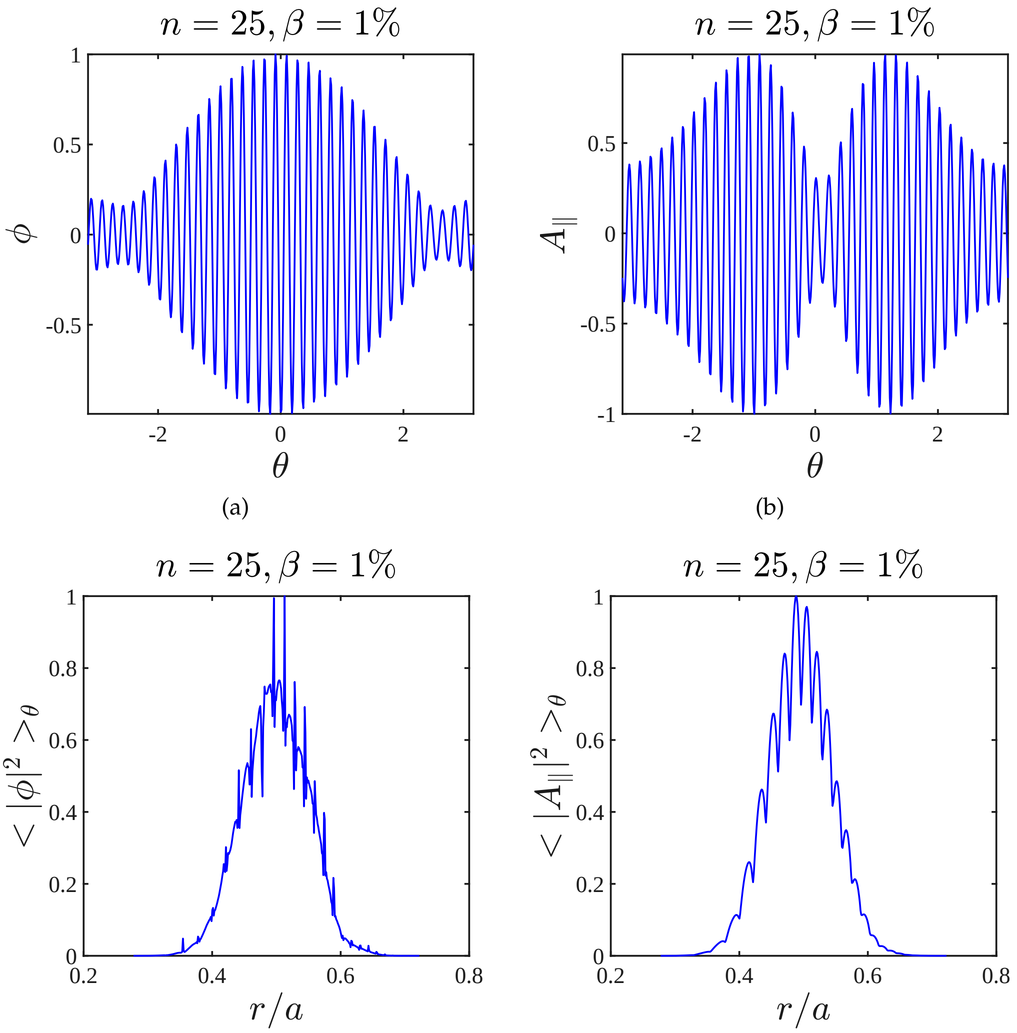

(a) (b)

(c) (d)

Figure 4: The structure of electrostatic potential (left) and vector potential (right) for $n=25$, with (a), (b) as a function of the poloidal angle at $r/a=0.5$ and (c), (d) as radial profile of the poloidally averaged squared fluctuations. The maximum amplitudes are normalized to 1.

in the vicinity of the rational surfaces [9, 15] are also observed. Similarly, we can also observe consistency between the 2D mode structures of the electrostatic potential and magnetic vector potential at $n=50$ of TEM in both NLT (Fig. 5) and GENE (Fig. 13 shown in Ref. [12]). In contrast to the structure shown in Fig. 3(a), the mode structure of the vector potential of TEM mode is ballooning-like, and the eddy structures of both the electrostatic potential and parallel vector potential are more localized. These results are consistent with those given in Ref. [12], reflecting the accuracy of NLT in solving linear electromagnetic drift wave instabilities.

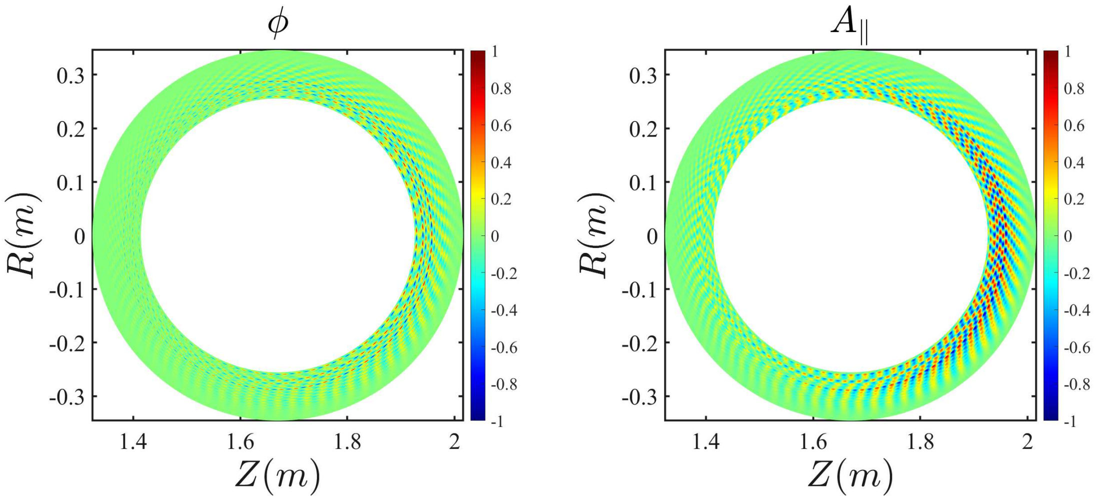

(a) (b)

Figure 5: 2D mode structure of the rescaled electrostatic potential (a) and parallel vector potential (b) in the (R,Z) plane for the case of $n=50$ with $\beta=1\%$.

4.2 Nonlinear simulation

NLT has been validated by the electrostatic nonlinear simulation of ITG dominated turbulence with adiabatic electron model [30, 33] and TEM dominated turbulence with gyrokinetic electron model [35]. In this section, we aim to further verify the reliability of the NLT code in simulating the nonlinear evolution of electromagnetic turbulence. Specifically, we compare the simulation results of nonlinear ITG turbulence under low-β conditions using the electromagnetic model with re-splitting technique and the electrostatic model with time diffusion method proposed in Ref. [35]. We expect that in this low-β limit, the magnetic perturbation on turbulence is small, and thus the two models should yield similar results.

In the context of these two cases, the reference temperature and simulation density are established at $T=1.97keV$ and $N=1.0\times10^{19}m^{-3}$, respectively, which correspond to $\beta(r=r_0)=0.2\%$. The radial simulation box spans from $0.2a$ to $0.8a$, where a is the minor radius. For both cases, simulations are performed only in a 1/3 wedge, and a total of 32 modes are retained, corresponding to $0\le k_y\rho_i\le1.39$, with $k_y=nq(r_0)/r_0$. The grid resolutions for $(n_x\times n_y\times n_z\times n_{v_\parallel}\times n_\mu)$ are fixed at $(256\times96\times16\times64\times16)$, and the time step is set at $\Delta t=1.5\omega_{ci}^{-1}$. The total simulation duration extends to approximately $100R_0/c_s$, with the sound speed $c_s=\sqrt{T_e/m_i}$. Additionally, we assume a mass ratio between ions and electrons of $m_i/m_e=400$ to expedite the simulation process.

Fig. 6(a) compares the time evolution of the radial heat diffusivity of ions and electrons in the electromagnetic and electrostatic simulations. Here, $\chi_{i(e)}=Q_{i(e)}/|\nabla T_{i(e)}|$,

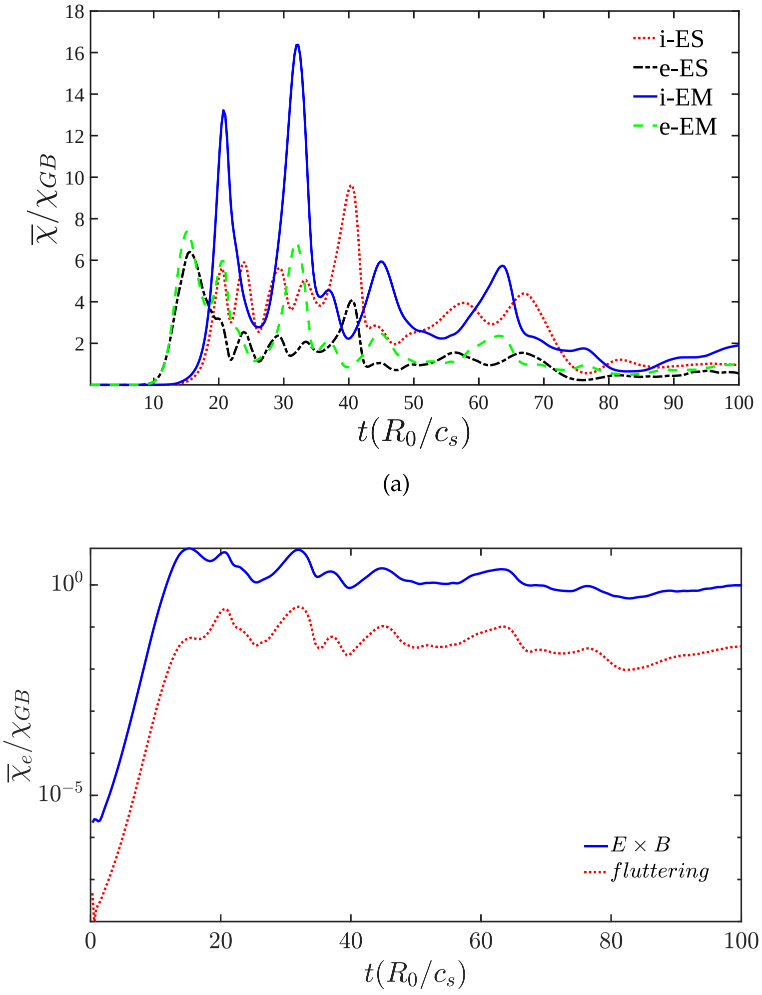

(a)

(b)

Figure 6: Evolution of radial heat diffusivity of ions and electrons over time. (a), comparison between electromagnetic (EM) case and electrostatic (ES) case; (b), comparison between "$E\times B$" component and "fluttering" component of the electron heat diffusivity in EM case.

where $Q_{i(e)}$ represents the particle heat flux of ions (electrons) averaged between the flux surfaces $r=0.4a$ and $r=0.6a$. χ is normalized by the gyro-Bohm unit $\chi_{GB}=\rho_i^2 v_{ti}/a$. As anticipated, under low-β conditions approaching the electrostatic limit, the electromagnetic and electrostatic simulations yield similar results. This is attributed to the lower magnetic perturbation in the electromagnetic simulation. As depicted in Fig. 6(b), the fluttering component of heat diffusivity due to the magnetic perturbation is significantly smaller than the $\boldsymbol{E}\times\boldsymbol{B}$ component caused by the disturbed electrostatic potential.

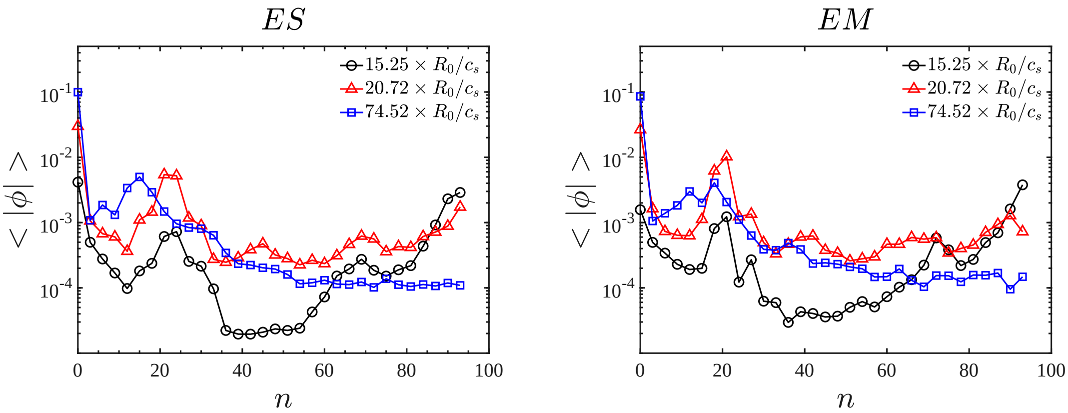

(a) (b)

Figure 7: Toroidal mode number spectrum of the electrostatic potential $\langle\phi\rangle \equiv \frac{1}{V}\int|\phi|$ for (a) ES case and (b) EM case at three different time points.

From Fig. 6(a), it can be observed that before $t = 18.41R_0/c_s$, the heat transport level of electrons is much greater than that of ions due to the higher growth rates of the electron drift wave instability. The electron heat transport reaches saturation first at $t = 15.25R_0/c_s$. After that, the level of electron heat transport gradually decreases, while the level of ion heat transport surpasses that of electrons and reaches saturation at $t=20.72R_0/c_s$. Correspondingly, the toroidal mode number spectrum of the electrostatic potential $\langle\phi\rangle \equiv \frac{1}{V}\int|\phi|d\boldsymbol{X}$ at three different moments, $t=15.25R_0/c_s$, $t=20.72R_0/c_s$, and $t=74.52R_0/c_s$, are shown in Fig. 7. Fig. 7(a) corresponds to the electrostatic case, while Fig. 7(b) corresponds to the electromagnetic case. A good agreement can be observed between the two cases under low-β conditions. In the quasi-linear stage, such as at $t=15.25R_0/c_s$ in the process, the spectral distribution of the electric potential is consistent with the growth rate spectral distribution shown in Fig. 2. The lowest mode values occur near the transition point of ITG-TEM. As turbulence evolves gradually, the process of inverse energy cascade becomes evident. The magnitude of high-n modes gradually decreases, while the energy of the modes near the transition point gradually increases. Ultimately, aside from the $n=0$ mode, the amplitude of the modes near $n=15$ is the highest, and as the value of n increases beyond 15, the amplitude of the modes gradually decreases.

Additionally, the mode structures of the turbulent component of the electrostatic potential in the (R,Z) plane for both the electrostatic (Fig. 8(a), Fig. 8(b) and Fig. 8(c)) and electromagnetic (Fig. 8(d), Fig. 8(e) and Fig. 8(f)) cases at different moments are shown in Fig. 8. With the evolution of turbulence, the non-$n=0$ components of the electrostatic potential transition from the "elongated" structure of electron drift waves with high n to the "short and thick" structure of ion drift waves, eventually being broken up by zonal

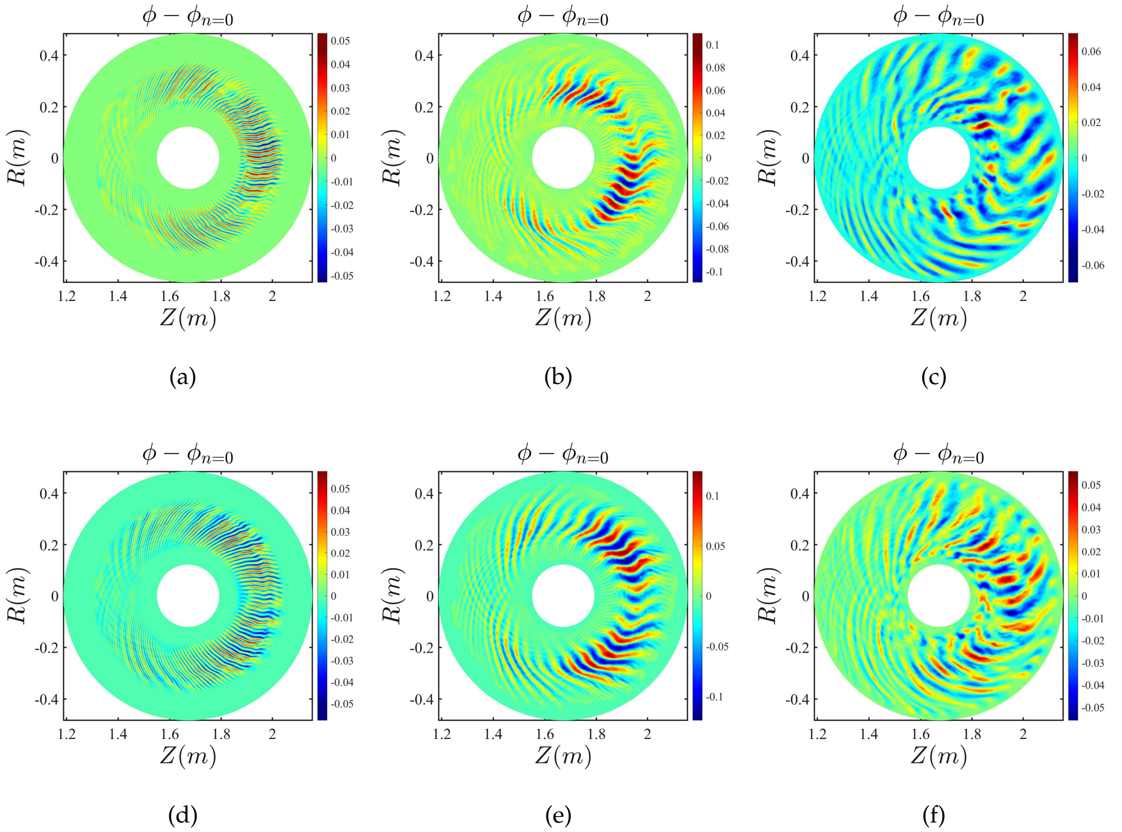

(a) (b) (c)

(d) (e) (f)

Figure 8: Mode structures of turbulent component of the electrostatic potential in the (R,Z) plane at three different time points, $t=15.25R_0/c_s$, $t=20.72R_0/c_s$ and $t=74.52R_0/c_s$. (a), (b) and (c) corresponds to ES case, (d), (e) and (f) corresponds to EM case.

flows. This process aligns with the previously discussed evolution in terms of radial heat diffusivity and the amplitude of the electrostatic potential.

To further assess the reliability of the electromagnetic model in calculating the zonal flow, the comparison between the time evolution of the $E\times B$ shear rates of the electrostatic case (Fig. 9(a)) and the electromagnetic case (Fig. 9(b)) is shown in Fig. 9. A well agreement is evident between the two cases. In both scenarios, the inward radial propagation of the electrostatic field and the fine scaled structures caused by the kinetic effects of the passing electrons around the rational surface can be observed.

5 Summary and discussion

In this study, we incorporated the re-splitting δf method [31] into the NLT code [34], which is a global semi-Lagrangian gyrokinetic code used for simulating electromagnetic

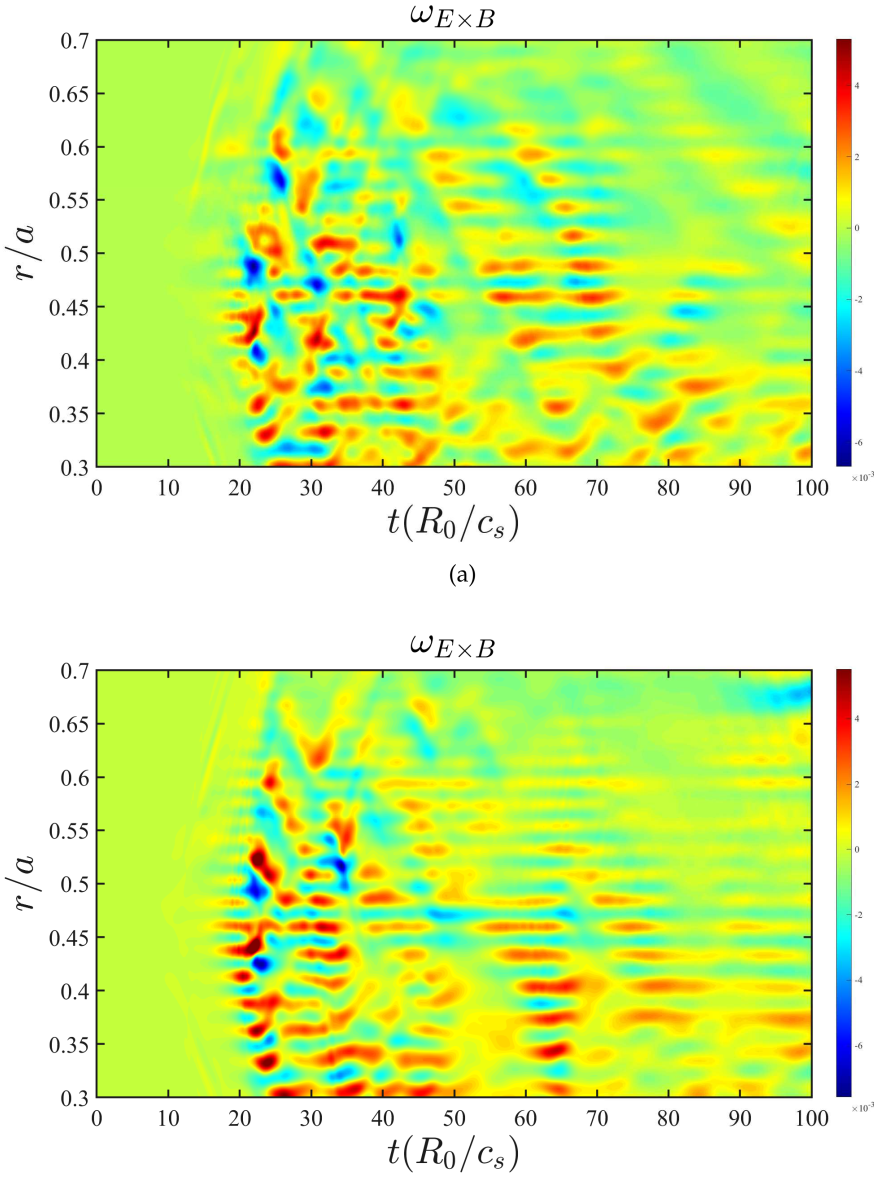

(a)

(b)

Figure 9: the time evolution of the $E\times B$ shear rates of (a) the electrostatic case and (b) the electromagnetic case.

micro-turbulence in tokamak plasmas. By combining the re-splitting δf method with the I-transform method [25–27], we have successfully mitigated the cancellation problem in the electromagnetic simulation of NLT. An additional advantage of this approach is that it does not necessitate significant modifications to the original model, specifically the numerical Lie transform method of NLT [29,34]. Comparing the results obtained from the NLT and GENE codes, we found reasonable agreement in terms of frequencies, growth rates, and mode structures of the linear instabilities (such as ITG, TEM, and KBM).

We also compared the electromagnetic simulation with the electrostatic simulation of ITG-dominated turbulence under low β conditions in NLT. The results from both models were well aligned at low β. Furthermore, we observed a transition from electron energy channels to ion energy channels in the nonlinear simulation. This is because the high-n TEM/ETG modes exhibit higher growth rates and reach saturation earlier compared to the ITG modes, as shown in Fig. 2 and Fig. 6. With this process, there is an inverse energy cascade from shorter-wavelength modes to longer-wavelength modes, depicted in Fig. 7.

It should be pointed out that for current the re-splitting method implemented in NLT code, it is often difficult to get a initial saturation in high-β or KBM regime with CBC parameters. This phenomena has also been reported in Ref. [24] as "high-β runaway". Recently, the nonlinear KBM simulation results have been reported [21] by using the ORB5 and EUTERPE codes with the mixed-variable scheme [22,23]. Note that although the re-splitting method can effectively solve the cancellation problem for $p_{\|}$-formulation, it can not resolve the CFL limitation caused by the fast parallel streaming of electrons. This requires other numerical methods to further enhance the numerical stability and accuracy, such as the split-weight scheme [6] and the mixed-variable and pull-back method [22,23]. And we would leave this work in the future.

Acknowledgments

This work was supported by the National Natural Science Foundation of China under Grant Nos. 12405275, the National MCF Energy R&D Program of China under Grant No. 2019YFE03060000 and 2022YFE03060004, Collaborative Innovation Program of Hefei Science Center, CAS under Grant 2022HSC-CIP008, the Strategic Priority Research Program of the Chinese Academy of Sciences (XDB0790201), and the CASHIPS Director's Fund under Grant No.YZJJ2023QN19. The numerical calculations in this paper were performed on ShenMa High Performance Computing Cluster in Institute of Plasma Physics, Chinese Academy of Sciences, Hefei advanced computing center and National Supercomputer Center in Tianjin.

References

[1] A. J. Brizard and T. S. Hahm. Foundations of nonlinear gyrokinetic theory. *Reviews of Modern Physics*, 79(2):421–468, 2007. Brizard, Alain/0000-0002-0192-6273 1539-0756.

[2] AJ Brizard and TS Hahm. Foundations of nonlinear gyrokinetic theory. *Reviews of Modern Physics*, 79(2):421, 2007.

[3] J. Candy and R.E. Waltz. An Eulerian gyrokinetic-Maxwell solver. *Journal of Computational Physics*, 186(2):545–581, 2003.

[4] Y. Chen and S. E. Parker. A delta f particle method for gyrokinetic simulations with kinetic electrons and electromagnetic perturbations. *Journal of Computational Physics*, 189(2):463–475, 2003.

[5] Yang Chen and Scott Parker. Gyrokinetic turbulence simulations with kinetic electrons. *Physics of Plasmas*, 8(5):2095–2100, 2001.

[6] Yang Chen and Scott E Parker. A δf particle method for gyrokinetic simulations with kinetic electrons and electromagnetic perturbations. *Journal of Computational Physics*, 189(2):463–475, 2003.

[7] M. D. J. Cole, A. Mishchenko, A. Bottino, and C. S. Chang. Tokamak ITG-KBM transition benchmarking with the mixed variables/pullback transformation electromagnetic gyrokinetic scheme. *Physics of Plasmas*, 28(3):034501, 03 2021.

[8] Julian Clark Cummings. *Gyrokinetic Simulation of Finite-Beta and Self-Generated Sheared-Flow Effects on Pressure-Gradient-Driven Instabilities*. Princeton University, 1994.

[9] J. Dominski, S. Brunner, T. Görler, F. Jenko, D. Told, and L. Villard. How non-adiabatic passing electron layers of linear microinstabilities affect turbulent transport. *Physics of Plasmas*, 22:062303, 2015.

[10] W Dorland, F Jenko, Mike Kotschenreuther, and BN Rogers. Electron temperature gradient turbulence. *Physical Review Letters*, 85(26):5579, 2000.

[11] X. Garbet, Y. Idomura, L. Villard, and T.H. Watanabe. Gyrokinetic simulations of turbulent transport. *Nuclear Fusion*, 50(4):043002, 2010.

[12] T. Görler, N. Tronko, W. A. Hornsby, A. Bottino, R. Kleiber, C. Norscini, V. Grandgirard, F. Jenko, and E. Sonnendrücker. Intercode comparison of gyrokinetic global electromagnetic modes. *Physics of Plasmas*, 23(7):072503, 2016.

[13] T. S. Hahm, W. W. Lee, and A. Brizard. Nonlinear gyrokinetic theory for finite-beta plasmas. *The Physics of Fluids*, 31(7):1940–1948, 1988.

[14] R. Hatzky, A. Könies, and A. Mishchenko. Electromagnetic gyrokinetic PIC simulation with an adjustable control variates method. *Journal of Computational Physics*, 225(1):568–590, 2007.

[15] Y. Idomura. A new hybrid kinetic electron model for full-f gyrokinetic simulations. *J. Comput. Phys.*, 313:511–531, 2016.

[16] R. Kleiber, R. Hatzky, A. Könies, A. Mishchenko, and E. Sonnendrücker. An explicit large time step particle-in-cell scheme for nonlinear gyrokinetic simulations in the electromagnetic regime. *Physics of Plasmas*, 23(3):032501, 03 2016.

[17] R. Kleiber, R. Hatzky, A. Könies, A. Mishchenko, and E. Sonnendrücker. An explicit large time step particle-in-cell scheme for nonlinear gyrokinetic simulations in the electromagnetic regime. *Physics of Plasmas*, 23(3):032501, 2016.

[18] WW Lee. Gyrokinetic particle simulation model. *Journal of Computational Physics*, 72(1):243–269, 1987.

[19] Zhixin Lu, Guo Meng, Roman Hatzky, Matthias Hoelzl, and Philipp Lauber. Full f and gyrokinetic particle simulations of Alfvén waves and energetic particle physics. *Plasma Physics and Controlled Fusion*, 65(3):034004, 2023.

[20] A. Mishchenko, A. Bottino, A. Biancalani, R. Hatzky, T. Hayward-Schneider, N. Ohana, E. Lanti, S. Brunner, L. Villard, M. Borchardt, R. Kleiber, and A. Könies. Pullback scheme implementation in ORB5. *Comput. Phys. Commun.*, 238:194–202, 2019.

[21] A. Mishchenko, A. Bottino, T. Hayward-Schneider, E. Poli, X. Wang, R. Kleiber, M. Borchardt, C. Nührenberg, A. Biancalani, A. Könies, E. Lanti, Ph Lauber, R. Hatzky, F. Vannini, L. Villard, and F. Widmer. Gyrokinetic particle-in-cell simulations of electromagnetic turbulence in the presence of fast particles and global modes. *Plasma Physics*

and Controlled Fusion, 64(10), 2022.

[22] Alexey Mishchenko, Michael Cole, Ralf Kleiber, and Axel Könies. New variables for gyrokinetic electromagnetic simulations. *Physics of Plasmas*, 21(5):052113, 2014.

[23] Alexey Mishchenko, Axel Könies, Ralf Kleiber, and Michael Cole. Pullback transformation in gyrokinetic electromagnetic simulations. *Physics of Plasmas*, 21(9):092110, 09 2014.

[24] RE Waltz. Nonlinear subcritical magnetohydrodynamic beta limit. *Physics of Plasmas*, 17(7), 2010.

[25] Shaojie Wang. Transport formulation of the gyrokinetic turbulence. *Physics of Plasmas*, 19(6):62504, 2012.

[26] Shaojie Wang. Kinetic theory of weak turbulence in plasmas. *Physical Review E - Statistical, Nonlinear, and Soft Matter Physics*, 2013.

[27] Shaojie Wang. Lie-transform theory of transport in plasma turbulence. *Physics of Plasmas*, 21(7), 2014.

[28] Xiaotao Xiao, Lei Ye, Yingfeng Xu, and Shaojie Wang. Application of high dimensional b-spline interpolation in solving the gyro-kinetic Vlasov equation based on semi-Lagrangian method. *Communications in Computational Physics*, 22(3):789–802, 2017.

[29] Yingfeng Xu, Zongliang Dai, and Shaojie Wang. Nonlinear gyrokinetic theory based on a new method and computation of the guiding-center orbit in tokamaks. *Physics of Plasmas (1994-present)*, 21(4):042505, 2014.

[30] Yingfeng Xu, Lei Ye, Zongliang Dai, Xiaotao Xiao, and Shaojie Wang. Nonlinear gyrokinetic simulation of ion temperature gradient turbulence based on a numerical Lie-transform perturbation method. *Physics of Plasmas*, 24(8):082515, 2017.

[31] Lei Ye and Yang Chen. Re-splitting δf method for electro-magnetic gyrokinetic particle-in-cell (PIC) simulation of tokamak plasmas. *Computer Physics Communications*, 250:107050, 2020.

[32] Lei Ye, Xiaotao Xiao, Yingfeng Xu, Zongliang Dai, and Shaojie Wang. Implementation of field-aligned coordinates in a semi-Lagrangian gyrokinetic code for tokamak turbulence simulation. *Plasma Science and Technology*, 20(7):074008, jun 2018.

[33] Lei Ye, Xiaotao Xiao, Yingfeng Xu, Zongliang Dai, and Shaojie Wang. Implementation of field-aligned coordinates in a semi-Lagrangian gyrokinetic code for tokamak turbulence simulation. *Plasma Science and Technology*, 2018.

[34] Lei Ye, Yingfeng Xu, Xiaotao Xiao, Zongliang Dai, and Shaojie Wang. A gyrokinetic continuum code based on the numerical Lie transform (NLT) method. *Journal of Computational Physics*, 316:180–192, 2016.

[35] Pengfei Zhao, Lei Ye, and Nong Xiang. Time diffusion method for gyrokinetic simulation of electrostatic turbulence with kinetic electrons. *Computer Physics Communications*, 269:108114, 2021.